

# Particle diffusion and localized acceleration in inhomogeneous AGN jets - Part I: Steady-state spectra

Xuhui Chen<sup>1,2\*</sup>, Martin Pohl<sup>1,2</sup>, Markus Böttcher<sup>3,4</sup>

<sup>1</sup> *Institute of Physics and Astronomy, University of Potsdam, 14476 Potsdam-Golm, Germany*

<sup>2</sup> *DESY, Platanenallee 6, 15738 Zeuthen, Germany*

<sup>3</sup> *Centre for Space Research, North-West University, Potchefstroom 2520, South Africa*

<sup>4</sup> *Astrophysical Institute, Department of Physics and Astronomy, Ohio University, Athens, OH 45701, USA*

18 November 2014

## ABSTRACT

We study the acceleration, transport, and emission of particles in relativistic jets. Localized stochastic particle acceleration, spatial diffusion, and synchrotron as well as synchrotron self-Compton emission are considered in a leptonic model. To account for inhomogeneity, we use a 2D axi-symmetric cylindrical geometry for both relativistic electrons and magnetic field. In this first phase of our work, we focus on steady-state spectra that develop from a time-dependent model. We demonstrate that small isolated acceleration region in a much larger emission volume are sufficient to accelerate particles to high energy. Diffusive escape from these small regions provides a natural explanation for the spectral form of the jet emission. The location of the acceleration regions within the jet is found to affect the cooling break of the spectrum in this diffusive model. Diffusion-caused energy-dependent inhomogeneity in the jets predicts that the SSC spectrum is harder than the synchrotron spectrum. There can also be a spectral hardening towards the high-energy section of the synchrotron spectrum, if particle escape is relatively slow. These two spectral hardening effects indicate that the jet inhomogeneity might be a natural explanation for the unexpected hard  $\gamma$ -ray spectra observed in some blazars.

**Key words:** galaxies: active – galaxies: jets – radiation mechanism: nonthermal – acceleration of particles – diffusion

## 1 INTRODUCTION

The inner parts of relativistic jets in Active Galactic Nuclei (AGNs) are known to emit radiation in every energy band we can observe. The actual size and location of the emission region, e.g. those in blazars, are still under debate (Ghisellini & Tavecchio 2009; Marscher 2013). Their size and distance make them challenging to resolve with our current imaging capability, except maybe a few cases where mm-VLBI observations are paving the way to resolve the base of the jet (Lu et al. 2013; Doeleman et al. 2012). For this reason, many theoretical efforts concerning AGN jets assume homogeneous emission region as the source of the multiwavelength emission (e.g. Dermer et al. 2009).

However, increasing temporal coverage of multiwavelength data and modeling results begin to suggest that single-zone homogeneous models are not sufficient in describing the complex phenomena. The observation that the blazars exhibit variability as fast as 3~5 minutes (Albert et al. 2007; Aharonian et al. 2007), and the detection of  $\gamma$ -ray above 100 GeV from several flat-spectrum ra-

dio quasars (FSRQs) without signature of  $\gamma - \gamma$  absorption by soft photons in the broad-line region (MAGIC Collaboration et al. 2008; H.E.S.S. Collaboration et al. 2013; Aleksić et al. 2011), indicate that the  $\gamma$ -ray emission region is extremely small, and at the same time located at parsecs away from the central AGN engine. This would require an unusually small angle of collimation, if the emission region covers the entire cross-section of the jet. One resolution to this conflict is the hypothesis that the larger jet contains small high-energy regions, presumably resulting from turbulence that is generated locally, far way from the central black hole. Apparently, single-zone homogeneous models are not adequate to describe these scenarios. (See Marscher 2014, for an example of such turbulent blazar emission model.)

In the picture considering small-scale structures, fast escape of particles means that, the highest-energy particles could have already cooled before they can travel far, while particles with lower energy still survive and occupy significant larger regions. This consideration suggests that to account for the multiwaveband radiation signals of AGN jets, one must consider inhomogeneous models spanning certain scale ranges to cover both the acceleration region and the region with the escaped particles. Various efforts have been

\* chenxuhui.phys@gmail.com

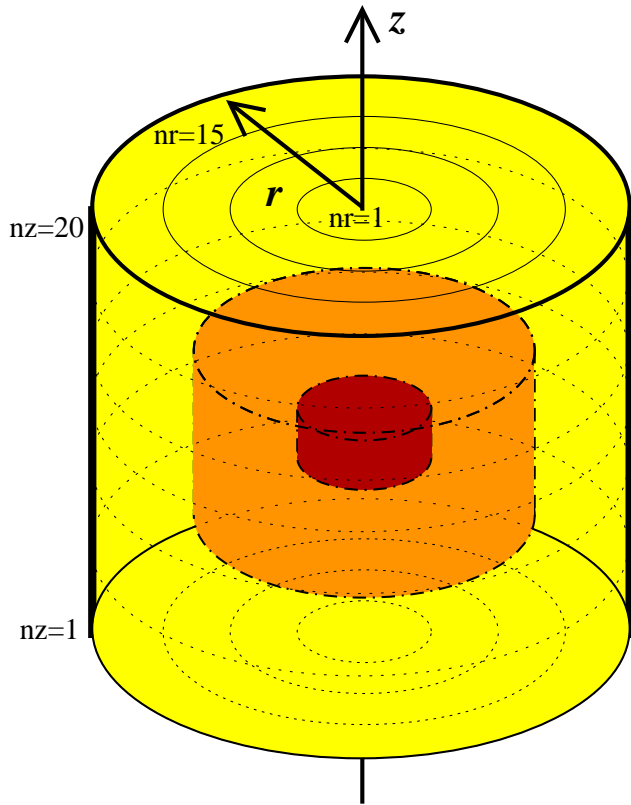


**Figure 1.** Sketch of the 3D geometry of the particle diffusion and localized acceleration in the axisymmetric cylinder. The red region represents the acceleration region where the acceleration is causing the particles to have the highest energy density. The spatial diffusion causes its surrounding regions to be still relatively energetic (orange zone), while in the yellow zone the particles have already cooled significantly. The actual particle distribution is shown in more detail in Fig. 5 and other figures as 2D maps.

made to model inhomogeneous jets (e.g. Ghisellini et al. 1985; Sokolov et al. 2004; Sokolov & Marscher 2005; Graff et al. 2008), although usually the details of the particle acceleration were not considered. Simplified approaches have been adopted to treat the acceleration region and the emission region separately (Kirk et al. 1998), although the emission from the acceleration region is not considered in their case. Recently, Richter & Spanier (2015) built a one-dimensional spatially-resolved model that accounts for the particle acceleration process, but the important light-travel-time effects (LTTEs) are not considered. Their geometry is suited for the laterally homogeneous shock structure, but not suitable for the study of 2D/3D small-scale structures such as turbulent acceleration regions.

The modeling of blazar SEDs usually requires very fast particle escape, considering the electron spectrum form required to match the observation. The required escape time scale is usually not much longer than the light-crossing time of the blazar emission region (Katarzyński et al. 2006; Chen et al. 2014). For this fast escape to be physically feasible, this escape should refer to escape from the accelerator, probably some smaller-scale structures (Giannios 2013) within the emission region. Particles experience cooling and diffusion, but no acceleration outside of these regions. Throughout this paper, we will call the entire region of the jet contributing to the blazar radiation ‘emission region’. The smaller sub-region where particle acceleration takes place is referred to as ‘ac-

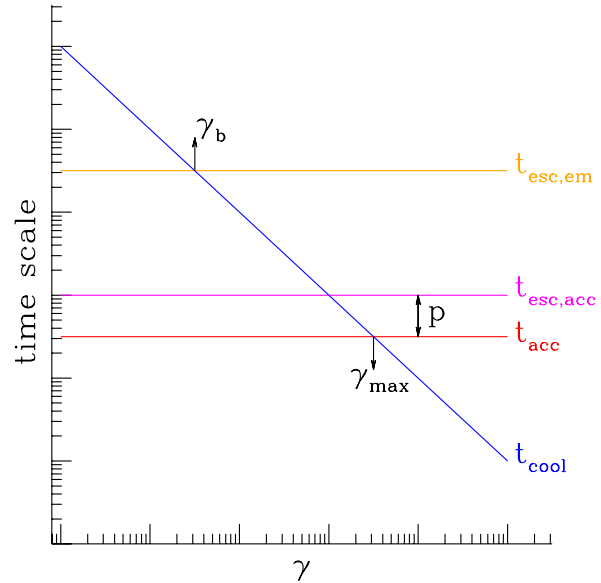


**Figure 2.** A sketch of the relationship between various time scales related to particle acceleration, cooling, and escape.

celeration region’, while the rest of the ‘emission region’ takes the name ‘diffusion region’.

Particle acceleration mechanisms that predict localized acceleration confined in small regions include magnetic reconnection (Guo et al. 2014; Sironi & Spitkovsky 2014), which can be triggered through turbulence (Zhang & Yan 2011), as well as various acceleration mechanisms at the shock front (Blandford & Eichler 1987; Sironi & Spitkovsky 2011). The thin but extended structure of the shocks (e.g., internal, external, or standing shocks, Spada et al. 2001; Kirk et al. 1998; Nalewajko & Sikora 2009) means that they can facilitate fast particle escape, but in order to explain the fast variability in blazar emission, internal shocks produced very close to the jet base (Rachen et al. 2010), or shocks associated with mini-jets (Giannios et al. 2009) or, again, small scale turbulent structures (Marscher 2014), would be required.

Except the consideration of emission region structure and particle acceleration, another major focus of relativistic jet models has been the radiative mechanism. The SEDs of blazars usually consist of two components, with the first peaking between infrared to X-ray frequencies, while the second peaking between X-ray to  $\gamma$ -ray energies (Ulrich et al. 1997; Fossati et al. 1998). Both hadronic and leptonic models have been frequently discussed, and have been successfully applied to blazars in most cases (Böttcher et al. 2013). The two kinds of models agree in explaining the low-frequency (below ultra-violet or X-ray) component of the blazar emission as electron synchrotron emission, but differ in their interpretation of the origin of the high energy (above X-ray) component. In the hadronic models protons are responsible for the high energy radiation through processes such as proton synchrotron emission (Aharonian 2000; Mücke & Protheroe 2001), p-p pion production (Pohl & Schlickeiser 2000), or p- $\gamma$  pion production (Mannheim & Biermann 1992) with subsequent synchrotron emission of pion decay products (Mannheim 1993; Rachen 2000; Mücke et al. 2003). The leptonic models on the other hand assume that the electrons, and possibly also positrons, in addition to providing the low-frequency emission through synchrotron, are also

responsible for the high energy emission through inverse Compton (IC) scattering (e.g. Maraschi et al. 1992). Depending on whether the seed photons of these scattering are the synchrotron photons the leptons themselves produced, or photons with origin external to the jet, the leptonic models can be further classified into synchrotron self-Compton (SSC) models and external Compton (EC) models. The EC models can then differ from each other based on the various possible sources of external seed photons, such as the accretion disc (Dermer et al. 1992), the broad line region (Ghisellini & Madau 1996), or the dusty torus (Sikora et al. 2009). The complexity of the SSC models come from the mathematical treatment of the nonlinear cooling of electrons in the SSC process (Zacharias & Schlickeiser 2013; Zacharias 2014), which is further complicated by the light retardation of the synchrotron photons (part of LTTEs, see the discussion by Sokolov et al. 2004). Traditionally the SSC models are usually associated with BL Lac objects while the EC models are usually associated with FSRQs. This is because, by definition, external emission lines are readily seen in FSRQs, but not in BL Lacs (Ghisellini et al. 1998). But whether this distinction in radiation mechanism is real or not, remains to be an open question (Chen et al. 2012).

In order to study inhomogeneous jets, Chen et al. (2011) have built a 2D leptonic model that takes into account all the LTTEs, including the external ones that cause delayed observation of further-away cells, and the internal ones that cause delayed arrivals of synchrotron photons in the SSC scattering. The model has been applied to cases where the inhomogeneity is caused by plasma crossing a standing perturbation. In those cases the inhomogeneity is mostly along the longitude of the jet, while the radial structure remains largely homogeneous. Direct particle exchange between cells is also neglected, based on the fact that the Larmor radius of the electrons is sufficiently small, and the assumption that the magnetic field is highly tangled. However, the nature of particle diffusion is also dependent on the turbulence property of the magnetic field, which is poorly known. Under certain circumstances, the diffusion between cells can be very important.

In this work we extend the model of Chen et al. (2011) by implementing particle diffusion between cells, as one mechanism for realistic particle escape. Combined with our direct handling of the particle acceleration using the Fokker-Planck equation, we investigate both spatial and momentum diffusion of particles at the same time. For the first time, our modeling of the particle evolution and emission encompasses both particles inside the accelerator and those already escaped from the accelerator. A sketch of acceleration and emission regions is shown in Fig. 1. Although our model is a time dependent one, in this paper we focus on what kind of steady state spectra emerge from the time dependent solution, and how. The flare-related variations will be the topic of discussion in a forthcoming paper.

As a simplification that permits understanding some, but not all of the physics that is captured in the 2D model, we will first introduce a semi-analytical two-zone model in §2. The methods used in the 2D model will be described in §3, followed by the simulation results in §4. Discussion and conclusion can be found in §5 and §6.

Throughout this paper, we will use non-primed notations for the quantities in the jet frame, and primed ones for those in the observer's frame. Subscripts 'em', 'acc' and 'dif' are used to denote parameters for emission, acceleration and diffusion regions respectively.

## 2 A TWO-ZONE MODEL

We first discuss the particle and emission spectra resulting from a semi-analytical two-zone model, which treats the acceleration and diffusion regions as two separate model zones. In this two-zone model it is assumed that particles are injected and accelerated in a small spherical acceleration zone. Those particles escape, and are subsequently injected into a much larger diffusion zone that surrounds the acceleration zone. There is no particle acceleration in the diffusion zone, but radiative cooling and further particle escape do play a role. In the two-zone model we only account for the synchrotron cooling, while IC cooling is not considered. We calculate analytically, with the help of numerical integrations, the electron spectrum of particles in both the acceleration and the diffusion zones. Then we estimate the synchrotron and SSC emission from both zones. We take into account the synchrotron seed photons from both zones when calculating the SSC emission, under the spherical geometry where the acceleration zone sits in the center of the diffusion zone. The diffusion zone approximately generates a synchrotron photon energy density of  $3L_{s,dif}(\epsilon)/4\pi R_{dif}^2 c$  in both the acceleration and diffusion zones, with  $L_s(\epsilon)$  denoting the synchrotron Luminosity as a function of photon energy in units of electron rest energy. The same energy density caused by the acceleration zone is more inhomogeneous, and approximated as  $3L_{s,acc}(\epsilon)/4\pi R_{acc}^2 c$  in the acceleration zone, and  $3L_{s,acc}(\epsilon)/4\pi R_{dif}^2 c$  in the diffusion zone.<sup>1</sup> To match the cases we study in the 2D model, we choose  $R_{dif} = 8.25R_{acc}$ .

The calculation of the steady-state electron spectrum is described in Appendix A. Four time scales, namely the acceleration time scale  $t_{acc}$ , the cooling time scale  $t_{cool}$ , the escape time scale from the acceleration region  $t_{esc,acc}$ , and the emission region,  $t_{esc,em}$ , are important in determining the total electron energy distribution (EED). As illustrated in Fig. 2, the Lorentz factor  $\gamma_{max}$ , at which the high-energy cut off starts, is determined by a balance between  $t_{acc}$  and  $t_{cool}$ ; the Lorentz factor  $\gamma_b$ , at which there is a spectral break, is determined by the relationship between  $t_{esc,em}$  and  $t_{cool}$ ; the spectral index of the EED above the spectral break,  $p$ , is determined by the ratio between  $t_{acc}$  and  $t_{esc,acc}$ .

The synchrotron power and synchrotron spectrum are calculated in the same way as we will do in the 2D model (Chen et al. 2011). We follow Graff et al. (2008) of using the  $\delta$ -function approximation to get the IC emission through a simple integration, i.e.  $\epsilon_{IC} = \frac{4}{3}\gamma^2\epsilon_0$ , and using a step-function approximation for the Klein-Nishina effect (Thomson scattering for  $\gamma\epsilon_0 < 3/4$ ; no scattering for  $\gamma\epsilon_0 \geq 3/4$ ). With this approach, we integrate over the seed photon distribution to obtain

$$j_{IC}(\epsilon_{IC}, t) = \left(\frac{\sqrt{3}}{4}\sigma_T c\sqrt{\epsilon_{IC}}\right) \times \int_0^{\epsilon_{max}} n(\gamma, t)U(\epsilon_0, t)\epsilon_0^{-3/2}d\epsilon_0, \quad \gamma = \sqrt{\frac{3\epsilon_{IC}}{4\epsilon_0}} \quad (1)$$

where

$$\epsilon_{max} = \begin{cases} \frac{3\epsilon_{IC}}{4}, & \text{when } \epsilon_{IC} \leq 1, \\ \frac{3}{4\epsilon_{IC}}, & \text{when } \epsilon_{IC} > 1, \end{cases} \quad (2)$$

because of the Klein-Nishina effect.

<sup>1</sup> Since the considered acceleration zone is much smaller than the diffusion zone, we use  $R_{dif} \simeq R_{em}$  and  $t_{esc,dif} \simeq t_{esc,em}$ .

**Table 1.** The parameters used for the benchmark cases. The observation angle is always  $1/\Gamma$  so that the Doppler factor  $\delta$  is equal to the bulk Lorentz factor  $\Gamma$ . The volume height  $Z = 4R/3$  in all 2D cases.  $D_x$ ,  $t_{\text{esc,acc}}$  and  $t_{\text{esc,dif}}$  are not independent in the 2D model. Here  $D_x$  is an input parameter, while the other two are measured when the simulation reaches the steady state.

	two zone	closed	open
B(G)	0.3	0.3	0.3
$\delta$	33	33	33
$\gamma_{\text{inj}}$	33	33	33
$R(\text{cm})$	$0.75 \times 10^{16}$	$0.75 \times 10^{16}$	$0.75 \times 10^{16}$
$n_e(\text{cm}^{-3})$	2.07	30	2.07
$t_{\text{acc}}(R/c)$	0.267	0.4	0.267
$D_x(\text{cm}^2/\text{s})$	-	$1.9 \times 10^{24}$	$3.8 \times 10^{24}$
$t_{\text{esc,acc}}(10^5 \text{ s})$	0.84	-	0.84
$t_{\text{esc,dif}}(10^5 \text{ s})$	23.3	-	23.3

The resulting EEDs have a sharp cutoff at the highest energy. This is caused by the simplification of not considering radiative cooling in computing the electron spectrum in the acceleration zone. A direct high-energy cutoff on the particle spectrum in the acceleration zone is implemented based on a posterior consideration of the cooling. Since this cutoff also affects the particle number, especially when the spectrum is hard, we make a correction to the particle number density afterwards. This ensures that with the particle escape and particle injection considered, the total particle number is conserved ( $n_{e,\text{acc}}/t_{\text{esc,acc}} = Q$ ).

We guide our modeling using the SEDs of Mrk 421. But we restrict ourselves from matching the SEDs in details, to avoid excessive time spent on fine tuning of parameters. We also intend to keep our results generally applicable to different objects.

In a benchmark case for the two-zone model (Fig. 3, parameters listed in Table 1), the EED forms a typical broken power-law distribution, with a spectral break of  $\sim 1$  at  $\gamma \approx 3 \times 10^3$ . Because there is a concentration of higher-energy synchrotron photons in the acceleration zone, emitted by the higher-energy electrons in that same zone, the seed-photon field for the SSC is disproportionately strong for the highest-energy electrons. This preference of SSC scattering between the high-energy electrons and the high-energy photons causes the SSC spectrum to be harder than the synchrotron spectrum, especially at frequency below the SED peaks, above which Klein-Nishina effect begins to play a role. This effect is clearly visible in Fig. 3 right, where the spectral indices are measured to be -0.68 at 10 eV and -0.52 at 1 GeV.

In another case (Fig. 4) the particle escape time is three times longer. This results in a harder electron spectrum, which leads to a dominance in the spectrum at the highest energy by electrons in the acceleration zone. Looking at the EED from low energy to high energy, this shift of dominance causes a spectral hardening at the highest energy, because the un-cooled electron spectrum in the acceleration zone is harder than the cooled electron spectrum in the diffusion zone. This feature is clearly visible in Fig. 4 left. But it is less apparent in Fig. 4 right, because the SED is similar to a  $\gamma^3 N - \gamma$  representation, instead of the EED shown on the left which is a  $\gamma^2 N - \gamma$  representation. A careful examination of the synchrotron spectral index reveals that a slight hardening of the spectrum by 0.01 is still present in the synchrotron SED. A combination of this EED hardening and the above mentioned hardening of the SSC spectrum result in a very hard GeV spectrum with spectral index of about -0.3 (equivalent to a photon index of -1.3).

### 3 THE 2D MODEL

The semi-analytic two-zone model already shows some unique spectra features that are not captured in one-zone models. However, there are some significant simplifications in the analytic approach that limits the accuracy of the model, e.g. the neglect of radiative cooling in the acceleration zone, the return-flux for lower-energy particles from the diffusion zone to the acceleration zone, and the inhomogeneity within the acceleration and diffusion zones. Further more, the applicability of the analytic model is limited because it does not account for the LTTE, which is important especially in studies of variability.

Taking one step beyond the two-zone analytic model, in this section we will describe our time-dependent 2D numerical model we built to study the particle acceleration and spatial diffusion in inhomogeneous jets. We consider a 2-dimensional axisymmetric jet model that is built on the Monte-Carlo/Fokker-Planck (MCFP) code developed by Chen et al. (2011). This model employs an approach combining the Monte-Carlo (MC) method for photon tracking and scattering, and Fokker-Planck (FP) equation for the electron momentum evolution (hence the name MCFP). The full transport equation takes the form

$$\begin{aligned} \frac{\partial n(\gamma, \mathbf{r}, t)}{\partial t} = & -\frac{\partial}{\partial \gamma} \left[ n(\gamma, \mathbf{r}, t) \dot{\gamma}(\gamma, \mathbf{r}, t) \right] \\ & + \frac{\partial}{\partial \gamma} \left[ D(\gamma, \mathbf{r}, t) \frac{\partial n(\gamma, \mathbf{r}, t)}{\partial \gamma} \right] + Q(\gamma, \mathbf{r}, t) \\ & - \nabla \cdot \left[ D_x(\gamma) \nabla n(\gamma, \mathbf{r}, t) \right]. \end{aligned} \quad (3)$$

$n(\gamma, \mathbf{r}, t)$  is the differential number density of particles. The first term on the right hand side

$$\dot{\gamma}(\gamma, \mathbf{r}, t) = \dot{\gamma}_{\text{cool}}(\gamma, \mathbf{r}, t) + \dot{\gamma}_D(\gamma, \mathbf{r}, t), \quad (4)$$

includes both radiative cooling  $\dot{\gamma}_{\text{cool}}(\gamma, \mathbf{r}, t)$  and stochastic acceleration  $\dot{\gamma}_D(\gamma, \mathbf{r}, t) = \frac{\gamma}{t_{\text{acc}}}$  in the acceleration region, caused by momentum diffusion of particles. The dispersion effect of the diffusion is described by the second term, also applicable in the acceleration region only, where the diffusion coefficient is

$$D(\gamma, \mathbf{r}, t) = \frac{\gamma^2}{2t_{\text{acc}}}. \quad (5)$$

The third term represents the injection of particles. The fourth term is the spatial diffusion of particles.  $D_x(\gamma)$  is the spatial diffusion coefficient.  $D_x(\gamma)$  could easily be energy dependent in our calculation, but in this work we restrict our discussion to the energy independent situations to reduce the number of free parameters. This also implies that the momentum diffusion coefficient, which is associated with the spatial diffusion, should be proportional to  $\gamma^2$ , i.e.,  $t_{\text{acc}}$  should be energy independent (Shalchi 2012). Also, only under this assumption is the analytical solution used in the two-zone model available (See Appendix A). Restricting the 2D model to this assumption makes the comparison of the two models much easier. More discussion on energy dependent  $t_{\text{acc}}$  can be found in Tramacere et al. (2011).

We use operator splitting to treat the momentum terms and spatial terms separately. Without the spatial terms, the equation is reduced to the FP equation. The finite-difference method used to solve the FP equation is described in details in Chen et al. (2011). The spatial terms of the transport equation is handled using the finite-element method, where we calculate the flux at each spatial boundary, and use those fluxes to update the density in each cell.

The diffusion causes propagation of particles to neighboring

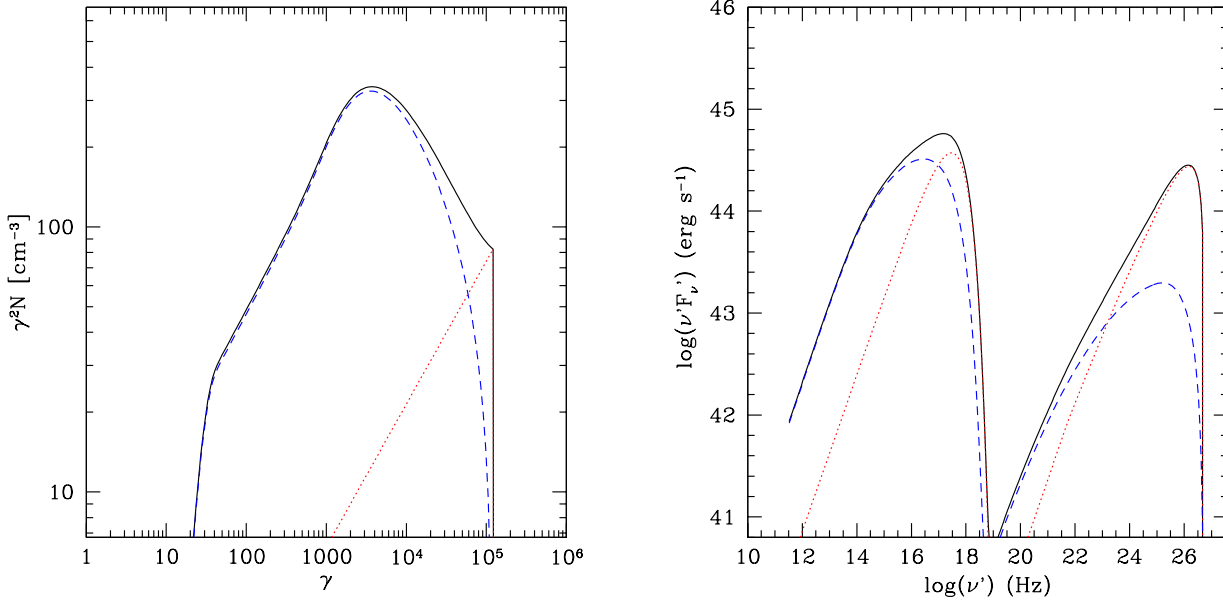


**Figure 3.** The EED and SED from the two-zone model. The parameters are chosen to match those of one case of the 2D model that will be discussed in §4.2.1. The total EED and SED are plotted with black solid lines, while the contributions from the acceleration zone and the diffusion zone are plotted in red dotted lines and blue dashed lines respectively. The spectral indices of the EED are  $-1.42$  at  $\gamma = 2 \times 10^2$  and  $-2.52$  at  $\gamma = 2 \times 10^4$ . The spectral indices of the SED are  $-0.68$  at  $10 \text{ eV}$  ( $2.42 \times 10^{15} \text{ Hz}$ ) and  $-0.52$  at  $1 \text{ GeV}$  ( $2.42 \times 10^{23} \text{ Hz}$ ).

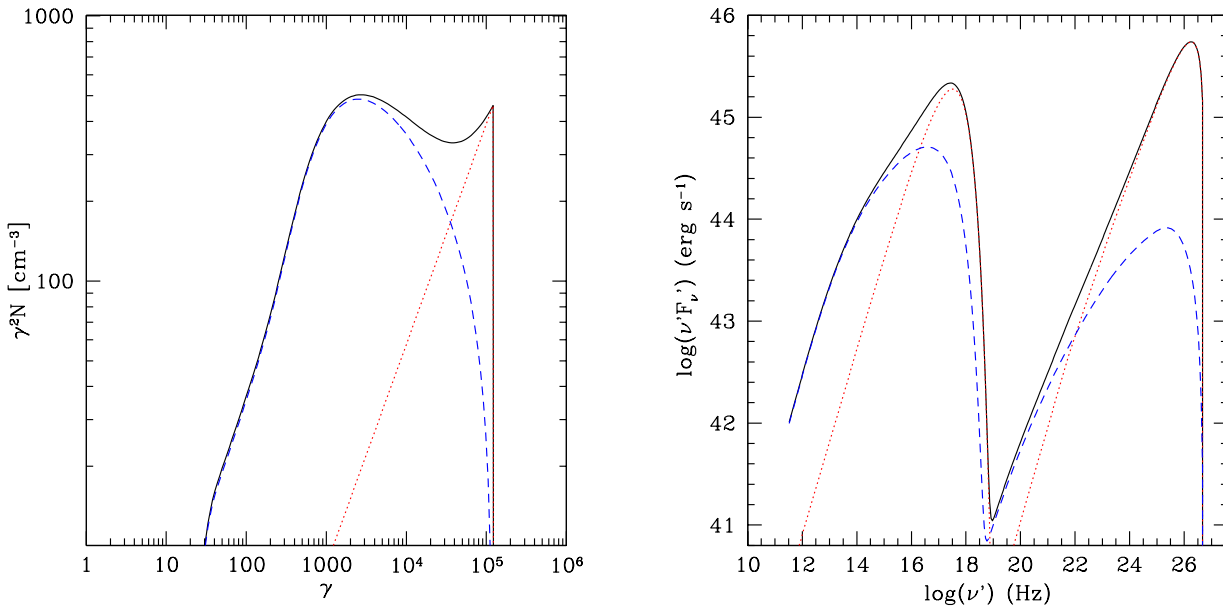


**Figure 4.** The EED and SED from the two-zone model, with relatively slow particle escape. The parameters are chosen to match those of one case of the 2D model that will be discussed in §4.2.2. The color scheme is the same as Fig. 3. The spectral indices of the SED are  $-0.597$  at  $10 \text{ eV}$  ( $2.42 \times 10^{15} \text{ Hz}$ ),  $-0.587$  at  $50 \text{ eV}$  ( $1.21 \times 10^{16} \text{ Hz}$ ) and  $-0.326$  at  $10 \text{ GeV}$  ( $2.42 \times 10^{15} \text{ Hz}$ ).

cells at every time step. The time step is set to be the light-crossing time of a single cell  $z/c$ , so the speed of particle escape and information exchange does not exceed the speed of light.

With spatial diffusion considered, we focus on the effects of localized particle acceleration, i.e., the acceleration region is a small accelerator. This acceleration region can occupy either one

or multiple cells in the 2D model, but is conceptually equivalent to the acceleration zone in the two-zone model. This acceleration can represent either second-order Fermi acceleration or acceleration by magnetic reconnection, in both of which the acceleration could be restricted to small turbulence regions.

In the 2D model we consider scenarios with reflecting (closed)

boundary condition (zero flux between the surface cells  $r = r_{max}, z = 1, z = z_{max}$  and the imaginary cells outside of the emission region) and escape (open) boundary condition ( $N(\gamma, \mathbf{r}, t) = 0$  at the imaginary cells; reflecting boundary condition is always used for the innermost boundary). In the former case the particle number is conserved, so the system will reach a steady state after a while. In the later case, the particles keep escaping from the emission region, with an implicit assumption that any particle outside of the emission region has negligible contribution to the emission. This is true for synchrotron radiation, if the magnetic field in outer regions are much weaker. It is also valid for SSC emission because of the lower synchrotron radiation density resulted from the weaker magnetic field. However, for EC emission, this assumption needs more careful examination. With particles continuously escape from the emission region, steady state only exists when there is additional source of particle pick up. This may happen at the same locations as the particle acceleration, because the turbulent magnetic field there may trap and isotropize particles in the intergalactic medium. In those cases, the trapped particles may have Lorentz factor similar to the bulk Lorentz fac-

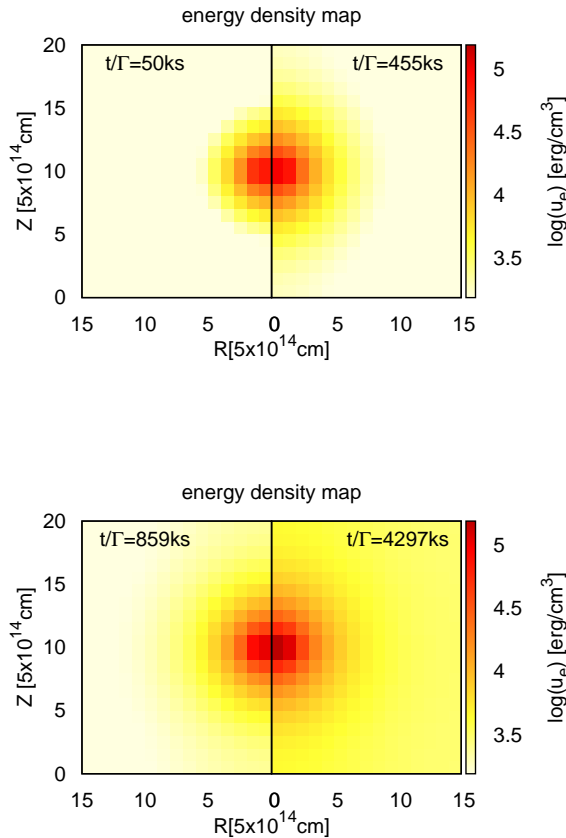


**Figure 5.** Energy density maps of the confined particle diffusion case at simulation time step 100, 900, 1700 and 8500 (corresponding to the electron energy distribution in Fig. 6 with color green, red, black and cyan). The color scheme spans two order of magnitude, and is normalized so that the highest density in the last figure is represented by dark red. The left/right halves of the figures show the maps at different time. The spatial unit ( $5 \times 10^{14}$  cm) is chosen to be equal to the grid size of the simulation.

**Table 2.**

boundary:	closed	open
centered acc.	§4.1.1, Fig. 5, 6 & 7	§4.2.1, Fig. 9 & 10
slow diffusion	§4.1.2, Fig. 8	§4.2.2, Fig. 11
off-center acc.	-	§4.2.3, Fig. 12, 13 & 14
elongated acc.	-	§4.2.4, Fig. 15

tor of the jet. This is how we choose  $\gamma_{inj}$  in our models. Effectively, this particle Lorentz factor determines the minimum Lorentz factor of the steady state EED in the open boundary scenario. In both the closed and open boundary scenarios, initially the emission regions have homogeneous particle distributions that form a power-law EEDs with spectral index -1.1 between Lorentz factor 1 and 33. This choice of initial particle distribution only affects the early evolution of the EED, it hardly has any effect on the final steady state spectra.

In this paper, our discussion focuses on SSC scenarios, even though some results may be generalized to EC scenarios as well, especially the results with closed boundary conditions, or if synchrotron emission is the primary subject of concern. Synchrotron-self absorption is also included in the 2D model, although it turns out to be not very important above 2 GHz in the cases discussed in this paper. All the simulation shown in this work use 20 layers in the longitudinal direction and 15 layers in the radial direction ( $n_z=20$  and  $n_r=15$ ). The length/radius ratio ( $Z/R$ ) is  $4/3$ , so the cell sizes in longitudinal and radial direction ( $dz$  and  $dr$ ) are the same. The simulation time step is chosen to be the same as the light crossing time of one cell ( $dz/c$ ).

## 4 2D RESULTS

With this time-dependent 2D model, we study the acceleration and diffusion of particles, as well as their synchrotron and IC emissions. The different cases we study, along with the associated section and figure numbers, are listed in Table 2.

### 4.1 Confined Particle Diffusion

In this section we discuss a closed emission volume, in which the particle diffuse spatially within a confined cylindrical region, while there is no particle exchange/escape at the outer-most boundary, i.e. the total particle number is conserved.

Similar cases discussed in this section cannot be studied with our two-zone model in §2, because in the two-zone mode we did not include the backflow of low energy particles from the diffusion region to the acceleration region. This backflow is important in the closed boundary case, because only with it, a particle number balance can be maintained between the acceleration region and the diffusion region.

#### 4.1.1 Localized acceleration in the center

In this case, in a central region with  $2 \times 2$  cells, particles are continuously accelerated through momentum diffusion. Subsequently the spatial diffusion in both  $z$  and  $r$  direction transports the high energy particles through the emission region. The time-dependent evolution of this process is shown in the electron energy density (equivalent to the area covered by a EED plot like those in Fig. 3 left) maps of Fig. 5.

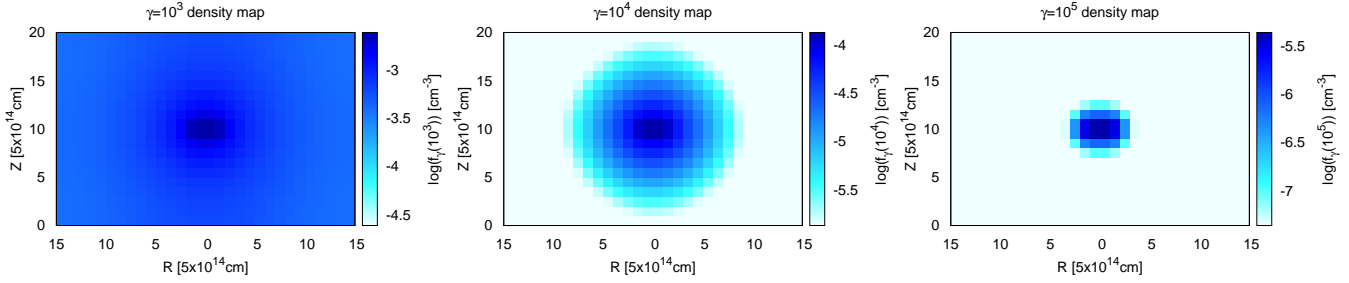


**Figure 6.** Density maps of the confined particle diffusion case at simulation time step 1700. They are maps of differential density  $N_\gamma$  for electrons with Lorentz factor  $10^3$ ,  $10^4$  and  $10^5$ . The left halves of the images are mirror image of the right halves to illustrate the cylindrical geometry.

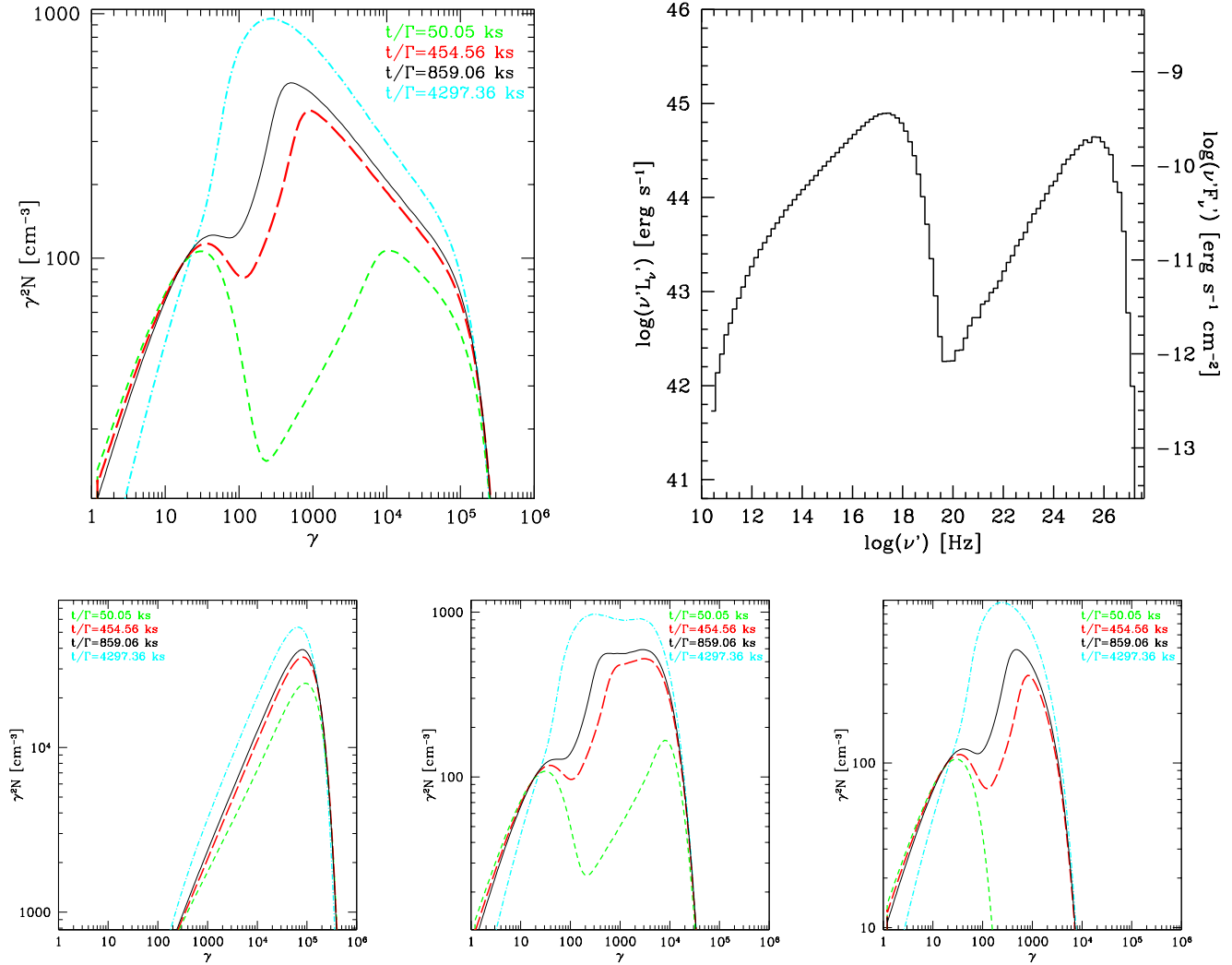


**Figure 7.** (Top) Total electron energy distribution (EED) and spectral energy distribution (SED). The SED have spectral indices  $-0.74$  at  $10$  eV, and  $-0.67$  at  $1$  GeV. (Bottom) The EED by individual cells. All of them are from the middle section in the longitudinal direction ( $jz=11$ ). Radially, they are (from left to right) from the inner, middle and outer cells ( $kr=1,8,15$ ).

The cyan line in the EED of Fig. 7 shows the distribution close to the steady state, after a long simulation time (8500 time steps). However, to save computer time, in most of the other cases in this work (except §4.1.2) we only run the simulation to the point of the black line (1700 time steps). This is enough for our purpose

of showing the difference between cases. For §4.2, those time is already more than enough for the simulation to reach a steady state.

The semi-steady total EED forms a broken power-law distribution where the slope before the break is close to 0. At early stages, the total EED shows two peaks, because it contains elec-

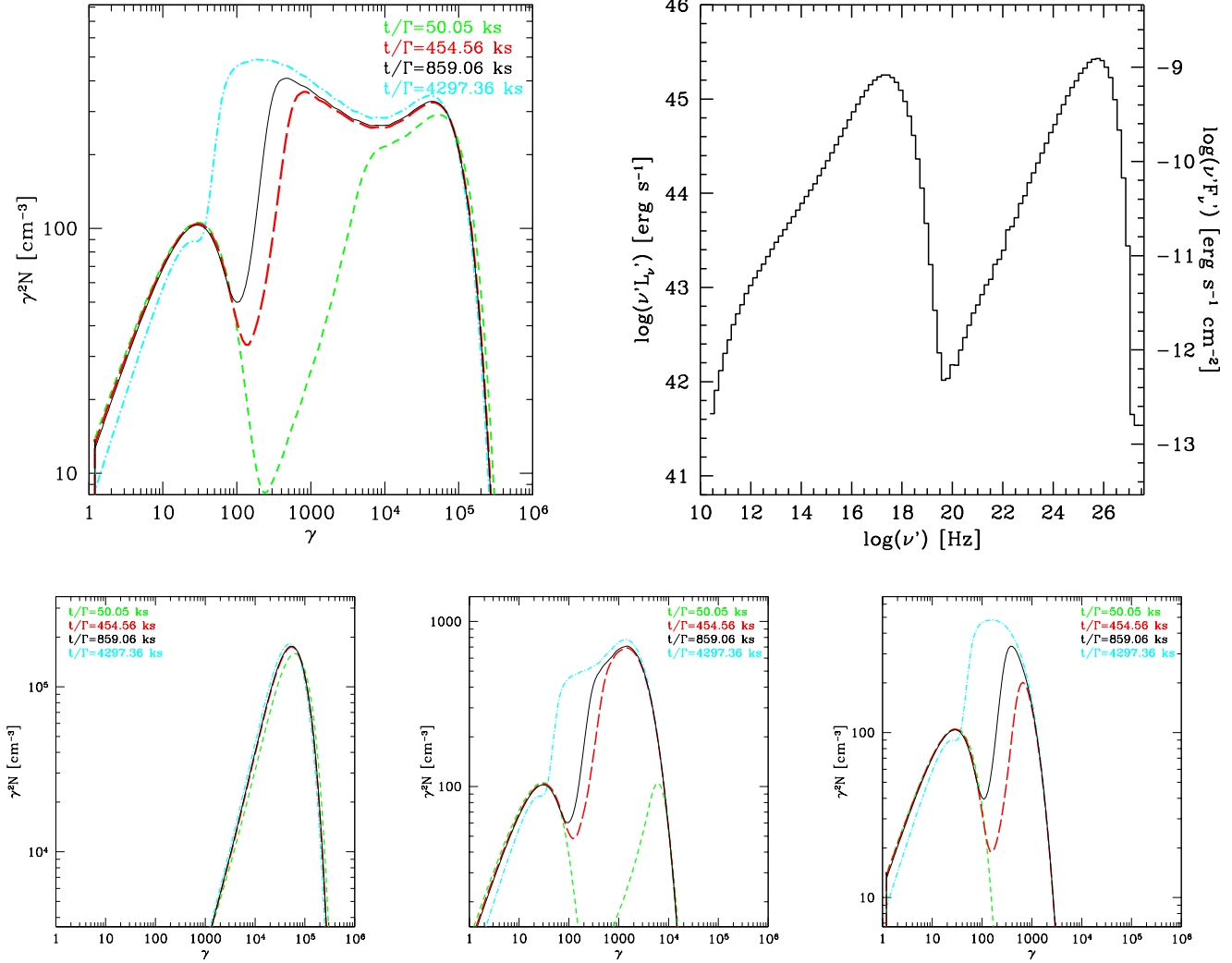


**Figure 8.** (Top) Total EED and SED for the case of §4.1.2 (closed boundary, slow diffusion, with acceleration in the central region; The SED have spectral indices  $-0.60$  at  $0.14$  eV,  $-0.51$  at  $50$  eV and  $-0.42$  at  $10$  GeV. (Bottom) The EED from the same individual cells as those in Fig. 7.

trons from different regions, in some of which the particles are accelerated, while in others the particles remain close to their initial distribution. We also show the SED that comes from the entire volume at late stages.

Single-cell EED from three sample cells are also shown (Fig. 7 bottom). The inner cell shows that the particles are accelerated to a power-law distribution with very hard spectrum. The EED with broken power-law distribution in the middle cell (cyan) is a result of the subsequent transport and cooling of those particles. In the outer cell, the particles had even more time to cool, therefore peak at lower energy compared to the middle cell.

This case is used as the benchmark case for the closed boundary scenario. Main parameters are shown in Table 1.

Because the particles are exposed to radiative cooling without further acceleration after they leave the central acceleration region, the highest-energy particles can only survive in a small central region. This region gets smaller with increasing particle energy (Fig. 6). This energy-dependent jet morphology means that, by making observation at different frequency, effectively we may be observing emission region of different size. The variability at

different energy may still be correlated, but there might be a significant difference in the light curves. More details of the variability pattern of the jet with localized acceleration will be discussed in a separate publication. The energy dependence also affects the SSC scattering. As we have already discussed in §2, the concentration of the most energetic photons and electrons in the center causes the SSC spectrum to be harder than the synchrotron spectrum. This feature is clearly seen in both the two-zone (Fig. 4 right) and the 2D (Fig. 11 upper-right) models, even though the confined diffusion scenario is quite different from the two-zone model. But it would not be expected in a one-zone model. This energy dependence also implies that even though the highest-energy photons are produced in a very compact region, the lower-energy photons, which may cause pair creation with the high energy photons, are less concentrated, thus alleviating the compactness constraint (Boutelier et al. 2008).

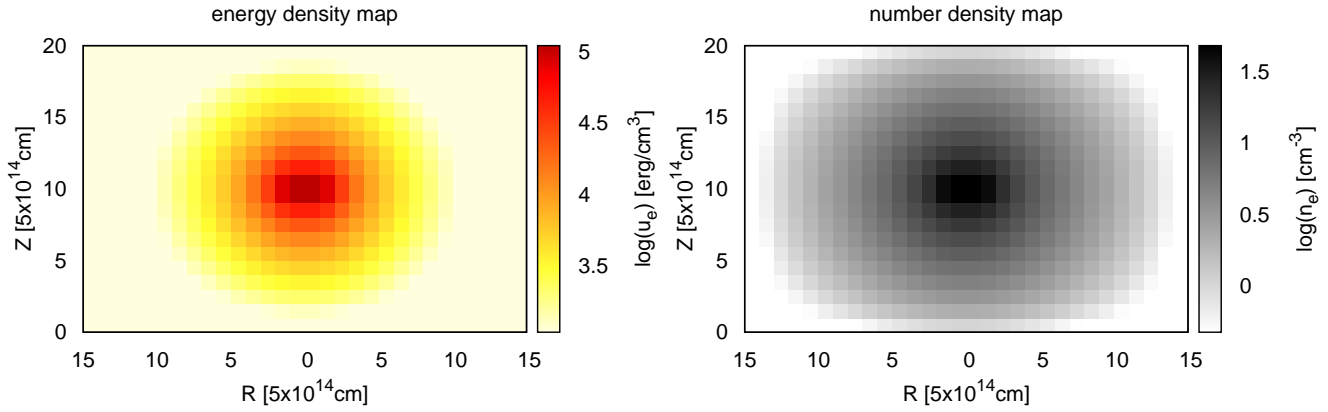


**Figure 9.** Density maps for the case of §4.2.1 (open boundary, acceleration in the center) at simulation time step 1700.

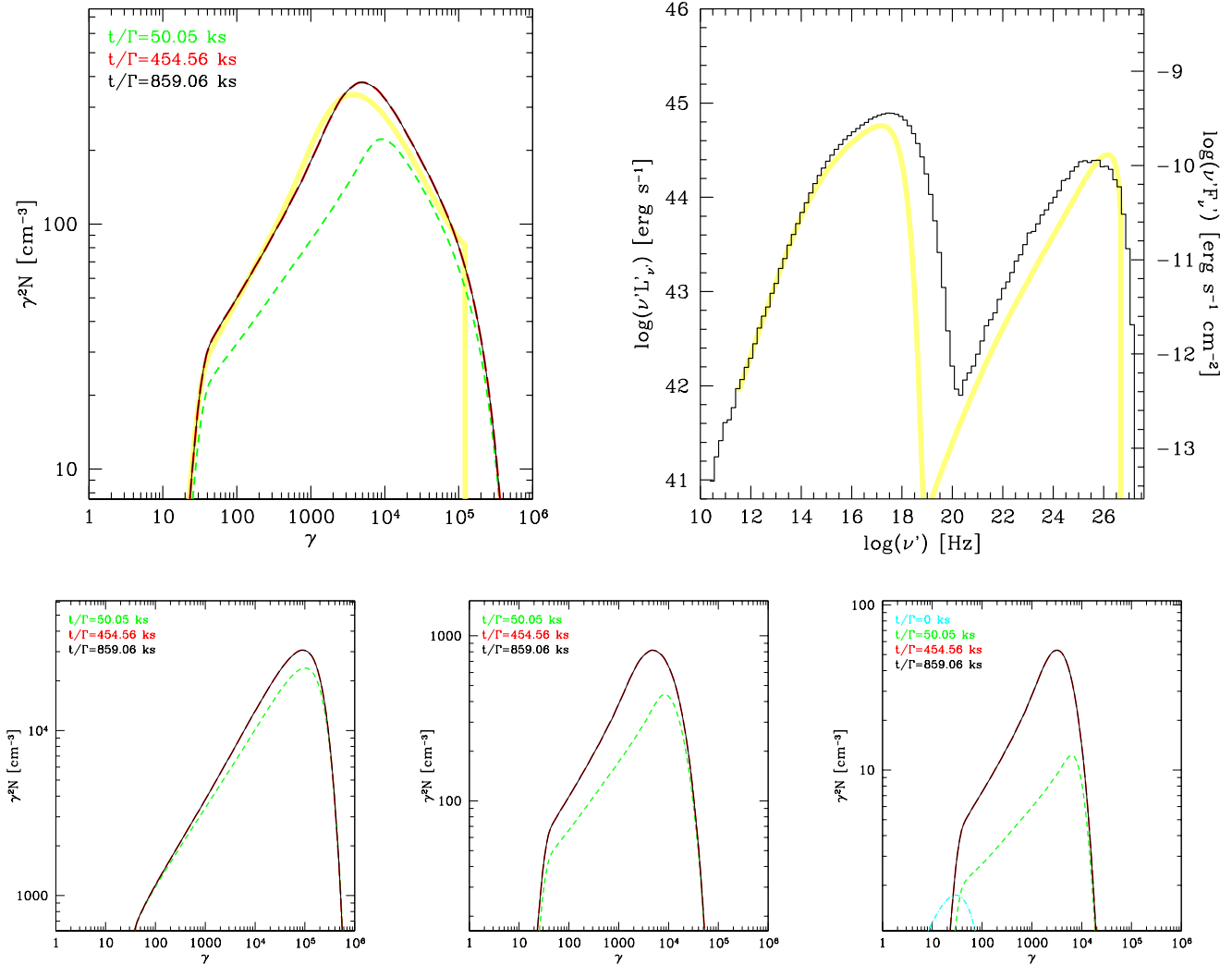


**Figure 10.** (Top) Total EED and SED for §4.2.1 (open boundary, acceleration in the center). The thick yellow lines are the EED and SED from the two-zone model (Fig. 3), plotted here for comparison. The spectral indices of the EED are  $-1.50$  at  $\gamma = 2 \times 10^2$  and  $-2.52$  at  $\gamma = 2 \times 10^4$ . The spectral indices of the SED are  $-0.63$  at  $10$  eV and  $-0.53$  at  $1$  GeV. (Bottom) The EED from the same individual cells as those in Fig. 7.

#### 4.1.2 Slow diffusion

In this case, the particle diffusion is less efficient compared to §4.1.1. This results in slower rate of particle escape from the acceleration region, and therefore harder EED (lower-left of Fig. 8). Similar to the two-zone model with slow particle escape (Fig. 4), the particles in the acceleration region have excess energy that provides an additional bump at the high-energy end of the total EED before cut off. The  $\gamma$ -ray spectrum is also extremely hard, with a spectral index of about -0.4 (equivalent to a photon index of -1.4) at 10 GeV. This kind of spectrum generally applies to localized acceleration with slow particle escape ( $t_{\text{esc,acc}} \gg t_{\text{acc}}$ ). The spectral hardening is another consequence of the energy-dependent inhomogeneity we show in Fig. 6. For slow particle diffusion, in which the high-energy bump is apparent, the power-law slope before the bump should always be close to 2, because it is the radiatively-cooled version of the  $p \sim 1$  spectrum resulted from inefficient particle escape.

## 4.2 Diffusive Particle escape

In this section the boundaries of the emission region are assumed to be open, i.e. the particles diffuse outside of the simulation box as if the density outside were zero. This implies a constant escape from the emission region, which is assumed to have a magnetic field stronger than its surroundings so that the emission from the surrounding region is negligible. We also assume that the acceleration region picks up particles from the intergalactic medium at a constant rate through the turbulent magnetic field.

We have chosen the parameters in the two-zone model (§2) so that they are directly comparable to the two cases in this section (§4.2.1 & §4.2.2). However, the total EEDs and SEDs are still slightly different, as can be seen in the comparison in Fig. 10 & 11. One of the reasons for the difference, for example, is that in the 2D model, the acceleration region contains more than one cell. The particle escape time for the central-most cell is longer than the escape time for the entire acceleration region, therefore some particles at the highest energy can have a harder spectrum in the 2D model. Another example is the posterior consideration of cooling in the acceleration zone of the two-zone model. This simplification leads to the sharp cut-off of EED and SED at the highest energy in the two-zone model, in contrast to the gradual cut-off in the 2D model.

#### 4.2.1 Localized acceleration in the center

The acceleration region is placed in the center of the emission region, similar to §4.1.1. In addition to the energy density map, we also show the particle number density map in Fig. 9. This illustrates how particles are picked up in the central region and then escape from the outer regions. The total EEDs (Fig. 10 upper-left) at later times overlap with each other, meaning that they have already reached a steady state. The steady EED shows a classic broken power-law distribution, with a cooling break of about 1 at  $\gamma = 10^3 - 10^4$ . This is consistent with what we saw in the two-zone model (Fig. 3). The SSC spectrum is also observed to be harder than the synchrotron spectrum, a feature already established in the two-zone model, and the closed boundary scenario. In Fig. 10 bottom we plot the EEDs for three different cells (in the center, mid-way between the center and the outer boundary, and the outer boundary, all at mid-way height in  $z$  direction.)

This case is used as the benchmark case for the open boundary scenario. Main parameters are shown in Table 1.

#### 4.2.2 Slow diffusion

We study the case with less efficient diffusion, similar to the case in §4.1.2, with the open boundary condition. In this scenario, we also observe the development of the high-energy bump in the EED, although it is not obvious in the SED (Fig. 11).

#### 4.2.3 Localized acceleration away from the center

In this section we study the cases where the acceleration region is not located at the center of the emission region. In the first case (Fig. 12), the acceleration region occupies the 3rd and 4th grid cells from the bottom. Except the location of the accelerator, the other parameters are identical to those in §4.2.1.

Because of the off-center position of the acceleration region, the whole emission region loses particles in different directions at a different rate. The particle escape happens on several time scales, and can no longer be described by a single escape time. One consequence of this non-uniform escape is, that the spectral break in the EED, which is a result of the competition between cooling and escape, no longer occurs at one specific energy. Instead, the spectrum gradually changes over a large range of electron energy that likely extends to the cut-off energy. If one were to measure the change in spectral index at the break, it would be less than 1, the number expected of radiative cooling. Because the proximity of the acceleration to the boundary, we also lose particles faster in general. This leads to a softer ‘uncooled’ spectrum (the one before the break). The EED with all these effects are shown in Fig. 12 bottom, with a comparison to the EED with acceleration region in the center. An exemplary attempt to measure the spectral change between  $\gamma = 2 \times 10^2$  and  $\gamma = 2 \times 10^4$  gives a break of 0.77. Compared to §4.2.1 the average electron density is adjusted to achieve similar SED and SSC cooling.

In order to test how the proximity of the acceleration to the boundary affects the total EED, we move the acceleration region closer to the boundary, occupying the 2nd and 3rd grid cells from the bottom (Fig. 13). The EED is shown in comparison with the case above. The measured spectral break becomes even smaller (0.71). Therefore we predict, if the acceleration region is located further away from the center than our model’s spatial resolution allows, the measured spectral break in the total EED may be significantly smaller than 1.

Another question we address is whether the location of the particle injection affects the spectral break. To answer this question we conceive a case where the particles are injected in the central region with 2x2 cells, while the acceleration region is located  $10^{15}$  cm (2 cells) away from the bottom boundary (Fig. 14). The resulted total EED shows a prominent bump at the injection energy  $\gamma = 33$ . But otherwise the EED is almost identical to that of Fig. 12 (the case with off center injection). We conclude that the spectral break is not affected by the location of the particle injection, but only by the location of the particle acceleration. However, this case is unlikely to represent the real picture of what happens in blazar jets, because it predicts a flux excess in radio frequency, which is not consistent with observation.

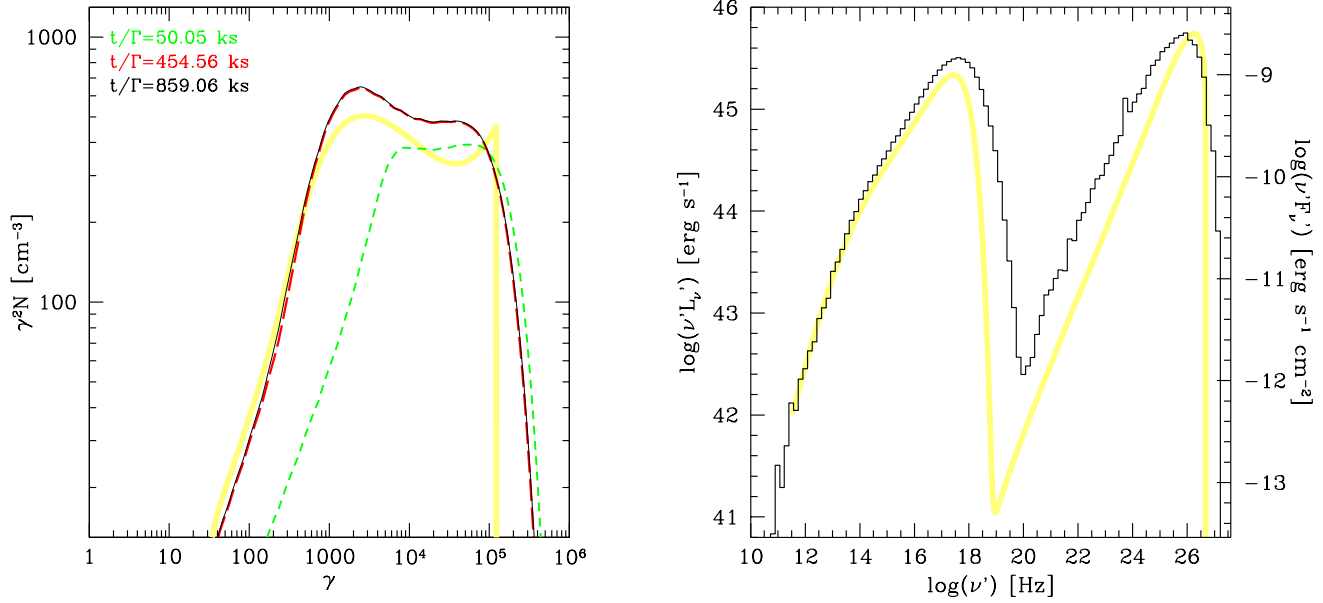


**Figure 11.** Total electron distribution and SED for §4.2.2 (open boundary, slow diffusion). The spectral indices of the SED are -0.57 at 10 eV, -0.56 at 50 eV and -0.48 at 10 GeV (due to the higher noise in the SED of this case, these estimation is done in a slightly broader frequency range compared to the other cases). The thick yellow lines are the EED and SED from the two-zone model with slow particle escape (Fig. 4), plotted here for comparison.

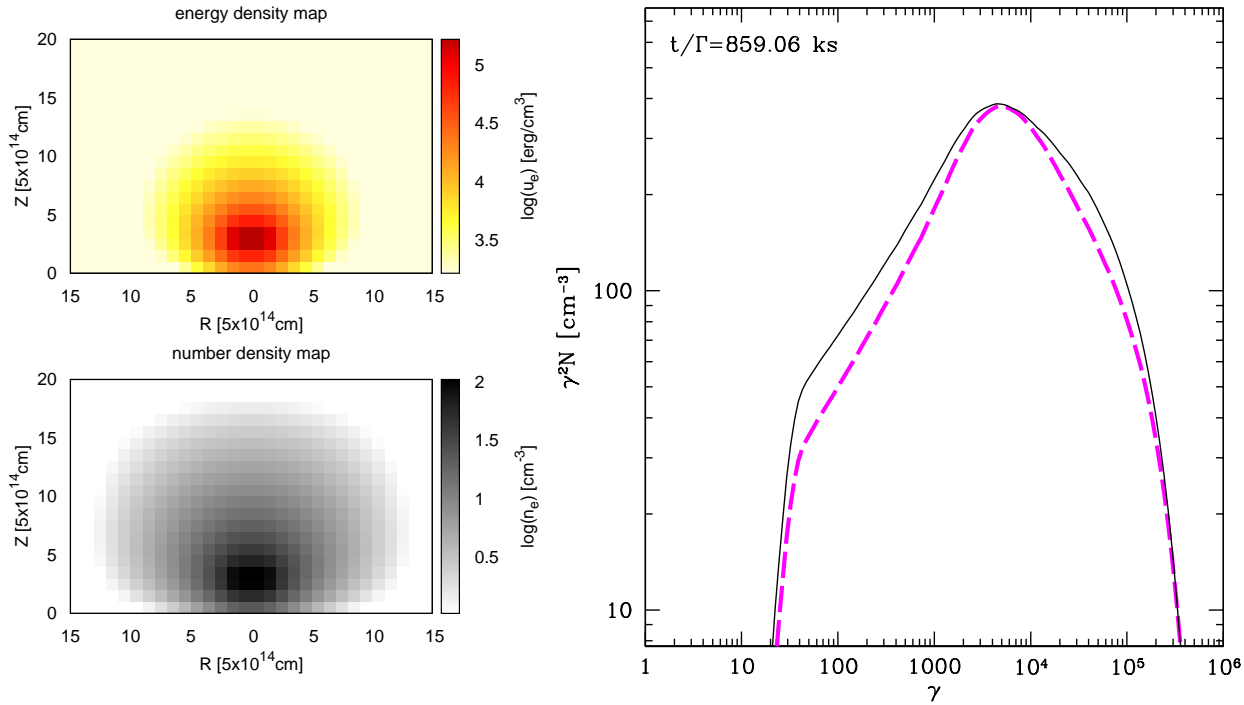


**Figure 12.** Density maps and total EED (black solid line) for the case of §4.2.3 (open boundary, acceleration away from the center) at simulation time step 1700. The spectral indices of the EED are -1.57 at  $\gamma = 2 \times 10^2$  and -2.34 at  $\gamma = 2 \times 10^4$ . The final EED shown in Fig. 10 is plotted here for comparison (magenta dashed line).

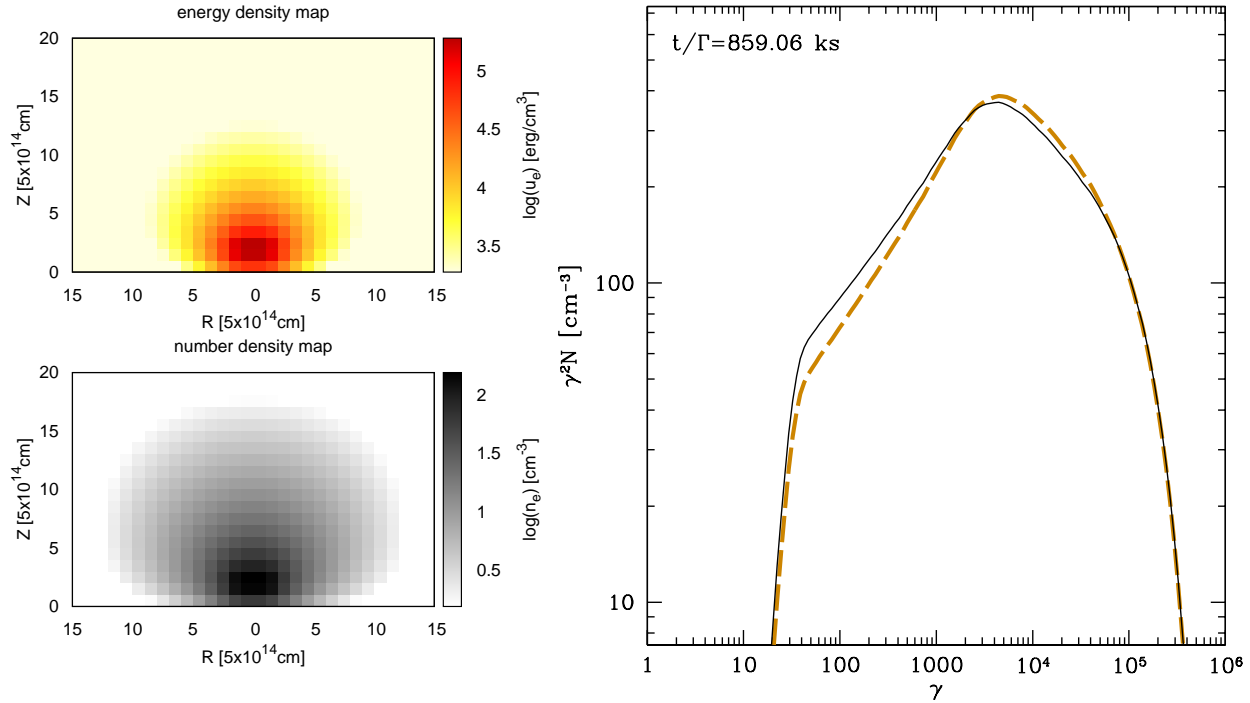


**Figure 13.** Density maps and total EED (black solid line) for the case of §4.2.3 (open boundary, acceleration away from the center) at simulation time step 1700. The acceleration region is further away from the center compared to Fig. 12. The spectral indices of the EED are  $-1.62$  at  $\gamma = 2 \times 10^2$  and  $-2.33$  at  $\gamma = 2 \times 10^4$ . The EED shown in Fig. 12 is plotted here for comparison (orange dashed line).

#### 4.2.4 Elongated acceleration region

Except the location of the accelerator, we also explore the effect of different geometry of the accelerator. In this case we construct an elongated accelerator with  $8 \times 1$  cells (Fig. 15 left). The total volume of the accelerator is the same as in §4.2.1. The other parameters are kept unchanged. The resulting EED (Fig. 15 right) has a slightly softer spectrum index both below and above the spectral break, while the break remains close to 1. This is caused by the more efficient escape from the accelerator under the current geometry with unchanged diffusion coefficient. However, without a reference spectrum, it is difficult to distinguish the spectrum from this case from those in §4.2.1. This result indicates that the geometry of the acceleration region has little impact on the EED. The choice of geometry does not affect our findings regarding the spectral breaks, or spectral hardening with increasing energy, as discussed in previous sections.

## 5 DISCUSSION

### 5.1 Spectral hardening at high energy

In both the closed and open-boundary scenarios, we notice the spectral hardening of the EED at high energy, if the particle diffusion is sufficiently slow (§4.1.2 & §4.2.2). This is a result of accounting for acceleration region and emission region at the same time. The acceleration region, which is small but dominates both the EED and the SED at high energy, has a harder spectrum compared to the emission region because of radiative cooling. This dominance in the synchrotron SED will be even stronger if we con-

sider a stronger magnetic field in the acceleration region. An exception is that if the magnetic field is so strong that the emission from the acceleration region dominates at all energies, the spectral hardening will no longer be present. If observations can measure the spectral index accurately enough, at a frequency close to but below the high energy cut off, we could search for this hardening of spectrum. Its existence will be evidence for localized particle acceleration and moderate particle escape being at play in AGN jets. A similar spectral hardening is not clearly visible in the SSC spectra. This might be related to the broadness of the seed photon spectra in the SSC scenario. Whether the spectral hardening for  $\gamma$ -rays can be more apparent in an EC scenario will be assessed in our future work. Interestingly, at very high energy (VHE, above 100 GeV)  $\gamma$ -ray, several blazars are already observed to show hardening of the spectra towards higher energy after the correction for extragalactic background light (EBL) absorption (MAGIC Collaboration et al. 2008; Archambault et al. 2014).

### 5.2 Hard SSC spectrum

In all our results, we observe the SSC spectra in the SED to be significantly harder than the synchrotron spectra at corresponding wavelengths. This is caused by the preference of IC scattering between high-energy synchrotron photons and high-energy electrons, because both of them are concentrated close to the accelerator in inhomogeneous jet models. This effect, combined with the hard EED in the cases with slow diffusion, provides a mechanism to produce

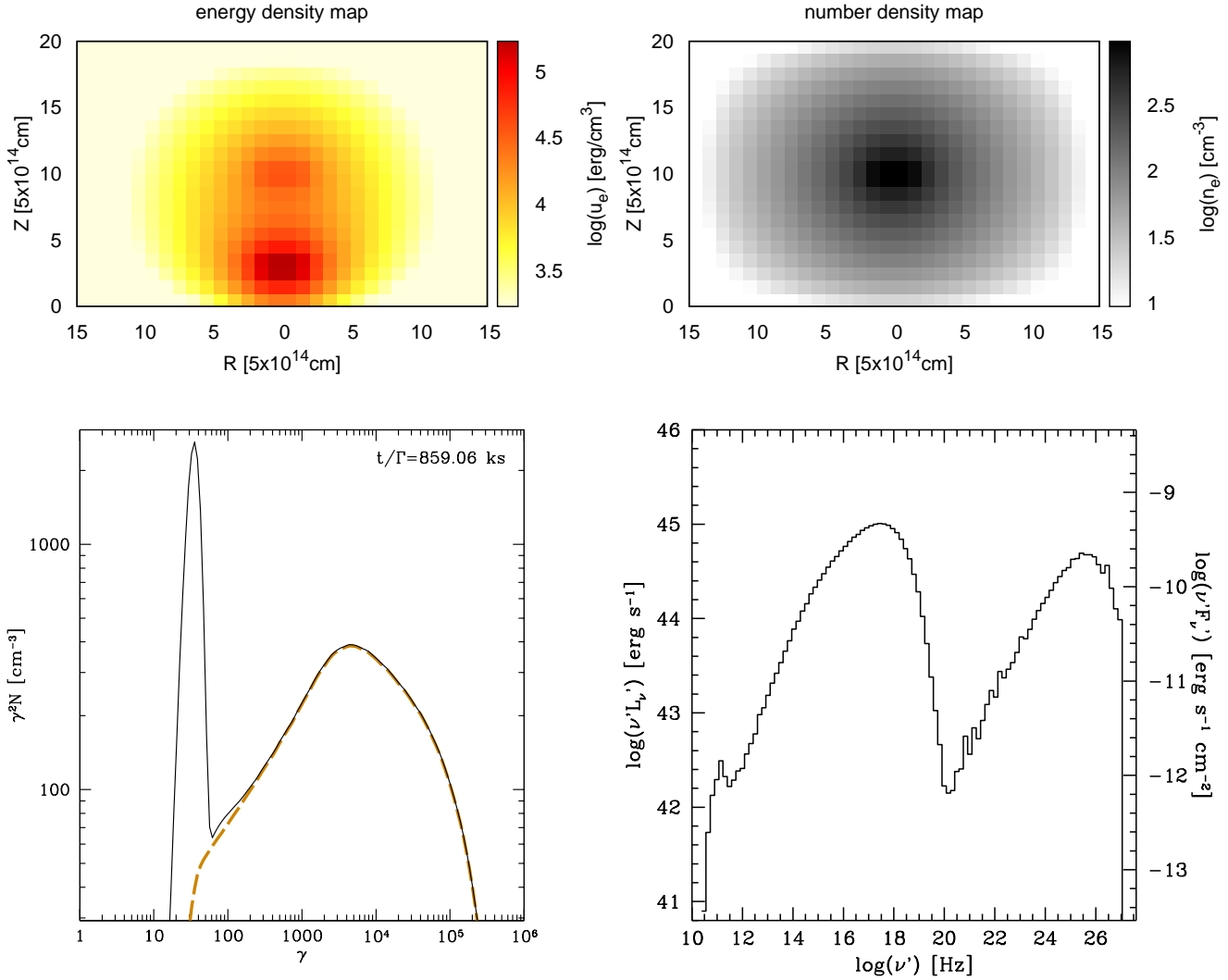


**Figure 14.** Density maps, total EED (black solid line) and SED for the case of §4.2.3 (open boundary, acceleration away from the center) at simulation time step 1700. The picking up of particles happens at the center of the emission region, not at the location of the acceleration region, which is what happens in Fig. 12. The spectral indices of the EED are  $-1.60$  at  $\gamma = 2 \times 10^2$  and  $-2.34$  at  $\gamma = 2 \times 10^4$ . The EED shown in Fig. 12 is plotted here for comparison (orange dashed line).

very hard spectra (photon index harder than  $-1.5$ <sup>2</sup>) at GeV energy at least (see §2 and §4.1.2). Since our choice of parameters is based on the SEDs of Mrk 421, a different parameter set might shift those hard spectra to even higher energy. Considering these effects, the inhomogeneous jet model might provide very important explanation for some of the unexpectedly hard VHE  $\gamma$ -ray spectra measured in several ‘high’-redshift VHE blazars after correction for the EBL absorption, and loosen the constraint these observations placed on the EBL (Aharonian et al. 2006).

<sup>2</sup> In a one-zone model, where the acceleration region is usually not accounted for, fast synchrotron loss preclude the power-law index of the electron spectra to be harder than  $-2$  regardless of the acceleration mechanism. This implies the photon index can not be harder than  $-1.5$ , under, again, one-zone assumptions (Aharonian et al. 2008).

### 5.3 Electron spectral break

Radiative cooling normally softens the electron spectrum by 1. A spectral break is expected to exist at the electron energy where  $t_{cool} = t_{esc,em}$ . Below this energy particles do not have enough time to cool before escape from the emission region, while above this energy, particles becomes softer because of the cooling effect. In the SED this break is expected to be 0.5 (Sari et al. 1998). However, the transition between uncooled and cooled spectra does not necessarily present itself as a clean cut broken power-law. In the open boundary scenario, we found (§4.2.3) that if the acceleration region is not located in the center of the emission region, the EED changes gradually over an energy range, and if measured as a broken power-law, the break may appear less than 1 (or 0.5 in the SED). If the observed power-law break in the SED is much larger than 0.5, it can not be explained by the cooling/escape break.

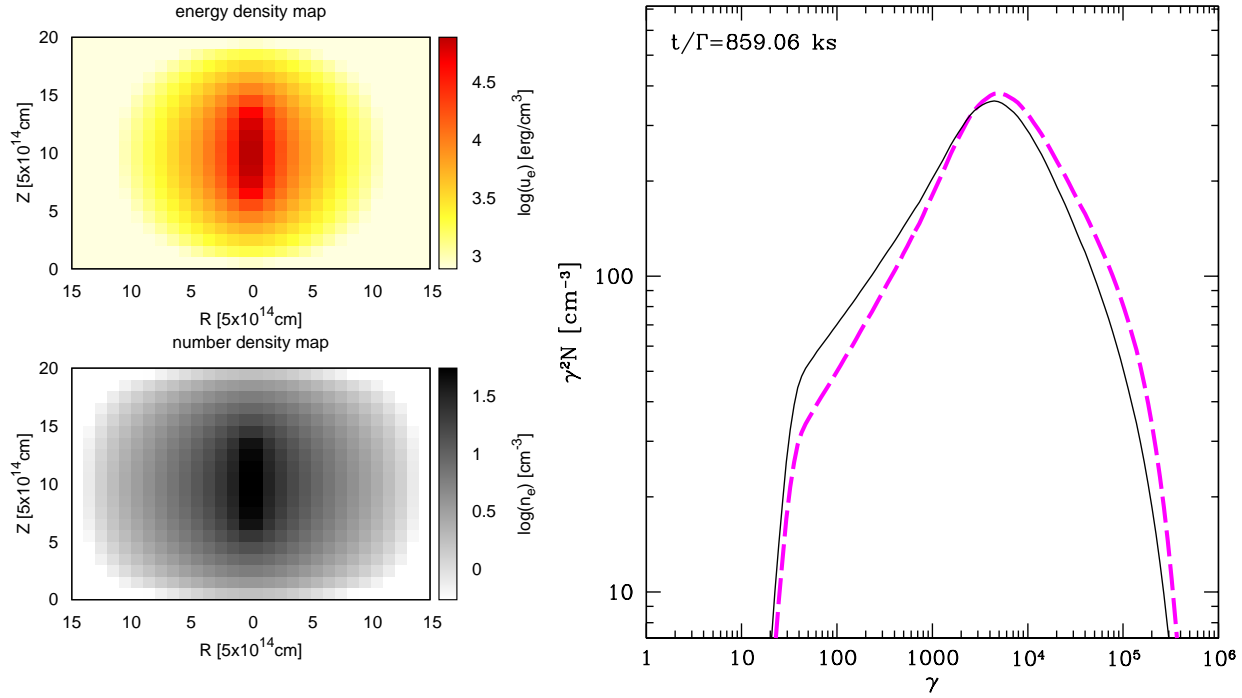


**Figure 15.** Density maps and total EED (black solid line) for the case of §4.2.4 (open boundary, elongated acceleration region) at simulation time step 1700. The spectral indices of the EED are -1.58 at  $\gamma = 2 \times 10^2$  and -2.63 at  $\gamma = 2 \times 10^4$ . The final EED shown in Fig. 10 is plotted here for comparison (magenta dashed line).

#### 5.4 Limitation of the simulation

Our simulation volume is divided into 20x15 cells. Higher-resolution simulations are possible but not practical because of the computational cost. The acceleration region in our model is therefore set to be of approximately 1/10 the length scale of the emission region, allowing it to occupy 2x2 cells. This limit on the acceleration region is only a numerical one, but not a physical constraint, i.e. the acceleration region can even be smaller, or located closer to the outer part of the emission region in AGN jets. Some of the phenomena observed in the current modeling work can be more significant if larger size ratio is considered.

## 6 CONCLUSIONS

We used our inhomogeneous time-dependent emission models to investigate the localized particle acceleration and spatial diffusion in AGN jets. This work focus on the steady-state spectrum and we summarize our findings as follows:

- (i) With the acceleration region much smaller than the emission region, the electrons form power-law/broken power-law distributions that adequately reproduce blazar SEDs with reasonable rates of particle escape;
- (ii) The inhomogeneity developed in the jet is energy-dependent, with higher-energy particles concentrated in smaller regions;
- (iii) The inclusion of particles both inside and outside of the acceleration region causes the EED/SED to show spectral hardening at high energy, if particle diffusion is slow;

(iv) The energy-dependent inhomogeneity causes the SSC spectrum to be harder than the synchrotron spectrum, and this might help to explain the very hard VHE spectra in several blazars.

(v) If the acceleration region is not located at the center of the emission region in an open-boundary scenario, the resulting EED forms an atypical broken-power-law distribution with spectral break less than 1;

(vi) The EED formed is weakly dependent on the geometry of the acceleration region.

## APPENDIX A

Let  $N_d(\gamma, t)$  denote the total number spectrum of particles in the diffusion (outer) zone, where escape is possible on time scale  $\tau_{\text{esc},d}$  and energy loss on time scale  $\tau_{\text{loss}} = 1/(a\gamma)$ , as for a dominance of synchrotron losses. The electron spectrum must satisfy the continuity equation

$$\frac{\partial N_d(\gamma, t)}{\partial t} - \frac{\partial}{\partial \gamma} \left( \frac{\gamma N_d(\gamma, t)}{\tau_{\text{loss}}} \right) + \frac{N_d(\gamma, t)}{\tau_{\text{esc},d}} = Q = \frac{N_a(\gamma, t)}{\tau_{\text{esc},a}}. \quad (6)$$

Here, we have already indicated that the source term  $Q$  is given by the rate of particle leakage out of the acceleration zone, for which  $N_a(\gamma, t)$  denotes the particle spectrum and  $\tau_{\text{esc},a}$  the escape time

scale. The general solution to equation 6 is given by

$$N_d(\gamma, t) = \frac{\tau_{\text{loss}}}{\gamma} \int_{\gamma}^{\infty} dq \int_{-\infty}^t dt' \delta\left(t - t' - \frac{1}{a\gamma} + \frac{1}{aq}\right) \times \frac{N_a(q, t')}{\tau_{\text{esc},a}} \exp\left(-\int_{\gamma}^q \frac{du}{au^2 \tau_{\text{esc},d}}\right). \quad (7)$$

For an energy-independent escape rate we can use the new momentum variable  $x = 1 - \gamma/q$  to simplify equation 7 to

$$N_d(\gamma, t) = \frac{\tau_{\text{loss}}}{\tau_{\text{esc},a}} \int_0^1 dx \int_{-\infty}^0 dt' \delta(t - t' - x\tau_{\text{loss}}) \times \frac{N_a\left(\frac{\gamma}{1-x}, t'\right)}{(1-x)^2} \exp\left(-x \frac{\tau_{\text{loss}}}{\tau_{\text{esc},d}}\right). \quad (8)$$

Note that the exponential is relevant only if the outer boundaries are open, because  $\tau_{\text{esc},d} = \infty$  and hence  $\exp(\dots) = 1$  for closed boundaries.

The delta functional in equation 8 is solved by  $x = (t - t')/\tau_{\text{loss}}$ , and so we can write

$$N_d(\gamma, t) = \frac{1}{\tau_{\text{esc},a}} \int_{t-\tau_{\text{loss}}}^t dt' N_a\left(\frac{\gamma \tau_{\text{loss}}}{\tau_{\text{loss}} + t' - t}, t'\right) \times \left(1 + \frac{t' - t}{\tau_{\text{loss}}}\right)^{-2} \exp\left(\frac{t' - t}{\tau_{\text{esc},d}}\right). \quad (9)$$

We now need the solution for the electron number spectrum in the acceleration zone,  $N_a(\gamma, t)$ . It obeys the continuity equation

$$\frac{\partial N_a(\gamma, t)}{\partial t} - \frac{\partial}{\partial \gamma} \left( \frac{\gamma N_a(\gamma, t)}{\tau_{\text{loss}}} - \frac{\gamma N_a(\gamma, t)}{\tau_{\text{acc}}} + \frac{\gamma^2}{2\tau_{\text{acc}}} \frac{\partial N_a(\gamma, t)}{\partial \gamma} \right) + \frac{N_a(\gamma, t)}{\tau_{\text{esc},a}} = Q_a. \quad (10)$$

Writing  $N_a(\gamma, t) = F_a(\gamma, t) \exp(-t/\tau_{\text{esc},a})$  and assuming that  $\tau_{\text{loss}} \gg \tau_{\text{acc}}$ , i.e. staying away from the loss-induced high-energy cut off in the spectrum, we can simplify equation 10 to

$$\frac{\partial F_a(\gamma, t)}{\partial t} + \frac{\partial}{\partial \gamma} \left( \frac{\gamma F_a(\gamma, t)}{\tau_{\text{acc}}} - \frac{\gamma^2}{2\tau_{\text{acc}}} \frac{\partial F_a(\gamma, t)}{\partial \gamma} \right) = Q_a \exp\left(\frac{t}{\tau_{\text{esc},a}}\right). \quad (11)$$

Under the condition  $\tau_{\text{acc}} \neq \tau_{\text{acc}}(\gamma)$  we can find Green's function for this problem in the literature (Kardashev 1962). With the source term on the right-hand side, the solution of equation 11 is

$$N_a(\gamma, t) = \frac{\sqrt{\tau_{\text{acc}}}}{\sqrt{2\pi}\gamma} \int_1^{\infty} d\gamma' \int_0^t dt' \frac{Q_a(\gamma', t')}{\sqrt{t-t'}} \exp\left(-\frac{t-t'}{\tau_{\text{esc},a}}\right) \times \exp\left(-\left[\sqrt{\frac{\tau_{\text{acc}}}{2(t-t')}} \ln \frac{\gamma'}{\gamma} + \frac{3}{2} \sqrt{\frac{(t-t')}{2\tau_{\text{acc}}}}\right]^2\right). \quad (12)$$

The differential number density of electron in the diffusion zone would be given by  $n_d(\gamma, t) = N_d(\gamma, t)/V_d$ , where  $V_d$  is the volume of the diffusion zone. Likewise,  $n_a(\gamma, t) = N_a(\gamma, t)/V_a$  is the differential density in the acceleration zone. When  $\tau_{\text{esc},d}$  is finite, the rate of transfer back into the acceleration zone is a small fraction of the total escape rate from the diffusion zone, which in the steady state itself is a lower limit to the escape rate from the acceleration zone. Therefore return flux is not an issue in open boundary situations modeled in a two-zone approach. In a closed boundary scenario, however, the total amount of escape and return particles are equal, and the return flux should be important.

## ACKNOWLEDGEMENTS

We thank the anonymous referee for constructive suggestions that helped improving the paper. XC and MP acknowledge support by the Helmholtz Alliance for Astroparticle Physics HAP funded by the Initiative and Networking Fund of the Helmholtz Association. MB acknowledges support from the South African Department of Science and Technology through the National Research Foundation under NRF SARChI Chair grant No. 64789.

## REFERENCES

- Aharonian, F. et al. 2007, *ApJL*, 664, L71  
 —. 2006, *Nature*, 440, 1018  
 Aharonian, F. A. 2000, *New Astronomy*, 5, 377  
 Aharonian, F. A., Khangulyan, D., & Costamante, L. 2008, *MNRAS*, 387, 1206  
 Albert, J. et al. 2007, *ApJ*, 669, 862  
 Aleksić, J. et al. 2011, *ApJL*, 730, L8  
 Archambault, S. et al. 2014, *ApJL*, 785, L16  
 Blandford, R., & Eichler, D. 1987, *Phys. Rep.*, 154, 1  
 Böttcher, M., Reimer, A., Sweeney, K., & Prakash, A. 2013, *ApJ*, 768, 54  
 Boutelier, T., Henri, G., & Petrucci, P.-O. 2008, *MNRAS*, 390, L73  
 Chen, X. et al. 2014, *MNRAS*, 441, 2188  
 Chen, X., Fossati, G., Böttcher, M., & Liang, E. 2012, *MNRAS*, 424, 789  
 Chen, X., Fossati, G., Liang, E. P., & Böttcher, M. 2011, *MNRAS*, 416, 2368  
 Dermer, C. D., Finke, J. D., Krug, H., & Böttcher, M. 2009, *ApJ*, 692, 32  
 Dermer, C. D., Schlickeiser, R., & Mastichiadis, A. 1992, *A&A*, 256, L27  
 Doleman, S. S. et al. 2012, *Science*, 338, 355  
 Fossati, G., Celotti, A., Ghisellini, G., Maraschi, L., & Comastri, A. 1998, *MNRAS*, 299, 433  
 Ghisellini, G., Celotti, A., Fossati, G., Maraschi, L., & Comastri, A. 1998, *MNRAS*, 301, 451  
 Ghisellini, G., & Madau, P. 1996, *MNRAS*, 280, 67  
 Ghisellini, G., Maraschi, L., & Treves, A. 1985, *A&A*, 146, 204  
 Ghisellini, G., & Tavecchio, F. 2009, *MNRAS*, 397, 985  
 Giannios, D. 2013, *MNRAS*, 431, 355  
 Giannios, D., Uzdensky, D. A., & Begelman, M. C. 2009, *MNRAS*, 395, L29  
 Graff, P. B., Georganopoulos, M., Perlman, E. S., & Kazanas, D. 2008, *ApJ*, 689, 68  
 Guo, F., Li, H., Daughton, W., & Liu, Y.-H. 2014, *ArXiv e-prints*  
 H.E.S.S. Collaboration et al. 2013, *A&A*, 554, A107  
 Kardashev, N. S. 1962, *Soviet Astronomy*, 6, 317  
 Katarzyński, K., Ghisellini, G., Mastichiadis, A., Tavecchio, F., & Maraschi, L. 2006, *A&A*, 453, 47  
 Kirk, J. G., Rieger, F. M., & Mastichiadis, A. 1998, *A&A*, 333, 452  
 Lu, R.-S. et al. 2013, *ApJ*, 772, 13  
 Mücke, A., & Protheroe, R. J. 2001, *Astroparticle Physics*, 15, 121  
 MAGIC Collaboration et al. 2008, *Science*, 320, 1752  
 Mannheim, K. 1993, *A&A*, 269, 67  
 Mannheim, K., & Biermann, P. L. 1992, *A&A*, 253, L21  
 Maraschi, L., Ghisellini, G., & Celotti, A. 1992, *ApJL*, 397, L5

- Marscher, A. P. 2013, in European Physical Journal Web of Conferences, Vol. 61, European Physical Journal Web of Conferences, 4001
- Marscher, A. P. 2014, *ApJ*, 780, 87
- Mücke, A., Protheroe, R. J., Engel, R., Rachen, J. P., & Stanev, T. 2003, *Astroparticle Physics*, 18, 593
- Nalewajko, K., & Sikora, M. 2009, *MNRAS*, 392, 1205
- Pohl, M., & Schlickeiser, R. 2000, *A&A*, 354, 395
- Rachen, J. P. 2000, in Proc. of GeV-TeV Gamma Ray Astrophysics Workshop: Towards a Major Atmospheric Cherenkov Detector VI, Snowbird, eds. B.L. Dingus, M.H. Salamon, D.B. Kieda, AIP Conf. Proc. 515 (New York: AIP), 41
- Rachen, J. P., Häberlein, M., Reimold, F., & Krichbaum, T. 2010, ArXiv e-prints
- Richter, S., & Spanier, F. 2015, *Astroparticle Physics*, 61, 102
- Sari, R., Piran, T., & Narayan, R. 1998, *ApJL*, 497, L17
- Shalchi, A. 2012, *Physics of Plasmas (1994-present)*, 19,
- Sikora, M., Stawarz, Ł., Moderski, R., Nalewajko, K., & Madejski, G. M. 2009, *ApJ*, 704, 38
- Sironi, L., & Spitkovsky, A. 2011, *ApJ*, 726, 75
- . 2014, *ApJL*, 783, L21
- Sokolov, A., & Marscher, A. P. 2005, *ApJ*, 629, 52
- Sokolov, A., Marscher, A. P., & McHardy, I. M. 2004, *ApJ*, 613, 725
- Spada, M., Ghisellini, G., Lazzati, D., & Celotti, A. 2001, *MNRAS*, 325, 1559
- Tramacere, A., Massaro, E., & Taylor, A. M. 2011, *ApJ*, 739, 66
- Ulrich, M.-H., Maraschi, L., & Urry, C. M. 1997, *ARA&A*, 35, 445
- Zacharias, M. 2014, *MNRAS*, 443, 3001
- Zacharias, M., & Schlickeiser, R. 2013, *ApJ*, 777, 109
- Zhang, B., & Yan, H. 2011, *ApJ*, 726, 90